Science Bulletin 64 (2019) 926–933

Contents lists available at ScienceDirect

Science Bulletin

journal homepage: www.elsevier.com/locate/scib

Science Bulletin
www.scibull.com

Article

In-situ incorporation of Copper(II) porphyrin functionalized zirconium MOF and TiO_2 for efficient photocatalytic CO_2 reduction

Lei Wang [a], Pengxia Jin [a], Shuhua Duan [a], Houde She [a], Jingwei Huang [a], Qizhao Wang [a,b,*]

[a] College of Chemistry and Chemical Engineering, Key Laboratory of Eco-Environment-Related Polymer Materials, Ministry of Education, Northwest Normal University, Lanzhou 730070, China
[b] School of Environmental Science and Engineering, Chang'an University, Xi'an 710064, China

ARTICLE INFO

Article history:
Received 9 April 2019
Received in revised form 9 May 2019
Accepted 14 May 2019
Available online 17 May 2019

Keywords:
Cu(II) tetra(4-carboxylphenyl)porphyrin (CuTCPP)
Metal-organic frameworks
Photocatalytic CO_2 reduction
TiO_2

ABSTRACT

As one of the highly effective methods to prepare catalysts for photocatalytic reduction of CO_2 into value-added chemicals, using metalloporphyrin as light-harvesting mixed ligand to modify metal-organic framework (MOF) is very valuable since it can greatly improve the prophyrin dispersibility and consequently inhibit its potential agglomeration. Herein, we employed a one-pot synthetic strategy to chemically immobilize Cu(II) tetra(4-carboxylphenyl)porphyrin (CuTCPP) into UiO-66 MOF structure through coordination mode. Meanwhile, in-situ growth of TiO_2 nanoparticles onto the MOF is actualized with the generation of CuTCPP ⊂ UiO-66/TiO_2 (CTU/TiO_2) composites. Under Xe lamp irradiation ($\lambda > 300$ nm), the catalytic result presents that an optimal value of 31.32 μmol g^{-1} h^{-1} CO evolution amount, about 7 times higher than that of pure TiO_2 was obtained through the photocatalysis. It is supposed owning to a consistent augment of light absorption derived from chemically implanted porphyrin derivative, which is simultaneously functioning with an efficacious separation of photo-induced carries given by the newly engendered composites between MOF and TiO_2, an effective catalytic activity and approving recyclability of CTU/TiO_2 can be achieved in the photocatalytic reduction of CO_2 into CO.

1. Introduction

Photocatalytic reduction of CO_2 into value-added chemicals is one of the most attractive techniques to resolve both environment issue and energy shortage [1]. Photo-synthesis in nature occurs mainly in highly ordered porphyrin pigments (chlorophylls). Interestingly, highly ordered porphyrin-based metal-organic frameworks (MOFs) can also perform similar behavior in promoting antenna-like light-harvesting characteristics [2,3]. In effect, MOFs have already drawn considerable attention in photocatalysis because of their distinctively chemical and structural diversity, extraordinary porosity, tailorable structures and CO_2 capture properties [4,5]. UiO-66, a typical MOF with the chemical formula of Zr_6 SBUs ($Zr_6O_4(OH)_4$), possesses satisfactory stability and is regarded as a potential photocatalyst. It is, however, generally incapable of accepting electrons from the BDC linker under light irradiation, because the redox potential energy level of the Zr_6 SBUs in UiO-66 lies above the LUMO of the BDC ligands and consequently lowers the electron accepting levels [6,7]. In order to engender new energy levels in the band structure, mixed ligand MOFs have been studied, and subsequently playing an essential role in the realization of MOFs' potential within a wide range of applications [8].

Cu(II) tetra(4-carboxylphenyl)porphyrin (CuTCPP), embracing a greatly conjugated macrocycle, can play the role of light-harvesting. It is exploited as a mixed ligand to simultaneously bind to metals together with another ligand so as to produce MOFs in possession of an integrally broadened light absorption. Moreover, the crystal structure and morphology of UiO-66 can be perfectly maintained after the mixed ligands, CuTCPP and BDC, jointly coordinating with Zr_6 SBUs to build a new MOF, CuTCPP ⊂ UiO-66 (CTU) [9–11]. It is worth noting that chemically implanting CuTCPP into UiO-66 is of great value in photocatalytic applications, since it is able to prevent CuTCPP from aggregation and self-quenching of the excited states as well as formation of catalytically inactive dimers, and therefore provide a consistent enhancement in light absorption for the actualization of an ameliorated photocatalytic ability than that of mere UiO-66 [12]. Actually, functionalized MOFs have already been explored as multifarious precursors in photo-assistant utilizations, such as hydrogen generation, degradation of organic pollutants, and CO_2 reduction [11,13–15].

In particular, MOF/semiconductor composites have increasingly attracted interest since they present great advantage of synergistic effect and consequently ameliorate photocatalytic performance

* Corresponding author.
E-mail address: wangqizhao@163.com (Q. Wang).

https://doi.org/10.1016/j.scib.2019.05.012
2095-9273/

with accelerated transfer of electrons [16]. TiO_2, a typical photocatalyst featuring high thermal and chemical stabilities, is commonly used to generate electrons and holes by sunlight irradiation in photocatalytic application. Unfortunately, this metallic oxide severely suffers a low CO_2 photoconversion efficiencies due to the undesired electron-hole recombination [17,18]. An effective approach to addressing such dilemma is to construct composites through integration of MOF structures and TiO_2 [14,19]. Resorting to this method, not only an improved CO_2 adsorption capacity given by the MOF component and the photo–excitation properties of the TiO_2 nanoparticles will be realized, but a significant abatement in the disadvantageous recombination of photo-induced carriers during photocatalysis can be also achieved due to the newly formed structures [20]. Herein, we combined TiO_2 nanoparticles and the mixed ligands, CuTCPP and BDC based MOF structure (CTU) via an in-situ hydrothermal procedure to integrate MOFs and inorganic semiconductors for the purpose of building CTU/TiO_2 nanocomposites. When playing the role of photocatalysts for CO_2 conversion driven by simulated solar light ($\lambda > 300$ nm), the optimal CTU/TiO_2 heterostructure presents considerably improved performance. The reduction rate of CO_2 into CO was up to 31.32 μmol g^{-1} h^{-1}, about 7 times that of the bare TiO_2. Besides the consistent augment of light absorption and tunable band gaps proffered by the incorporation, the separation of the photo-generated charge carriers can be also promoted through the formation of semiconductor-MOF composites during the photocatalytic reduction of CO_2 into CO. Furthermore, the possible mechanism supposed for its impressive photocatalytic performance is also presented.

2. Experimental

2.1. Materials

Pyrrole (Adamas Reagent Co., Ltd, 99.0%), 4-formylbenzoic acid (Adamas Reagent Co., Ltd, 99.0%) and propionic acid (Adamas Reagent Co., Ltd, 99.0%) were purchased from Damas-beta. Benzoic acid ($C_7H_6O_2$, 99.9%), copper(II)chloride dihydrate ($CuCl_2{\cdot}2H_2O$), zirconium (IV) chloride ($ZrCl_4$, 98%), terephthalic acid ($C_8H_6O_4$, BDC, 98%) and titanium (IV) butoxide ($C_{16}H_{36}O_4Ti$, 98%) were all purchased from Sinopharm Chemical Reagent Co. Ltd. Absolute dimethyl formamide (C_3H_7NO, DMF, 99.9%), ethanol and acetone were all purchased from Sinopharm Chemical Reagent Co. Ltd, which was used as both reaction and washing solvent. All reagents are analytical grade without further purification except pyrrole, which was purified by distillation under reduced pressure before each used.

2.2. Preparation of TiO_2

TiO_2 was synthesized using the same procedure according to the reported method [21]. 5 mL of titanium (IV) butoxide was added into 10 mL ethanol solution stirring for 1 h in ice bath. Afterwards, 6 mL mixed solution containing water and ethanol with the volume ratio of 1:4 was added to the reaction system and continuously stirred for another 1 h. Then, the reaction mixture was transferred to 50 mL teflon–lined steel autoclave and heated at 180 °C for 12 h, and afterwards cooled down naturally. The product was collected by centrifugation and consecutively washed with 10 mL of deionized water and ethanol for more than five times. The product was dried at 80 °C to give white solid powder.

2.3. Preparation of CuTCPP ⊂ UiO-66 (CTU)

TCPP and CuTCPP were synthesized according to our previous work [22]. Generally, CTU was synthesized according to the literature using a solvothermal method [12]. 30 mg $ZrCl_4$, 30 mg BDC, 10 mg CuTCPP and 0.5 g benzoic acid were added to 2 mL DMF. After vigorously stirring for 30 min, the mixture was put into 50 mL teflon-lined steel autoclave and heat at 130 °C for 12 h. The mixture was cooled down to room temperature and subsequently centrifuged to give a red solid. The solid was washed with DMF and acetone for at least three times, and then dried in an oven at 80 °C for 12 h. The synthesis of UiO-66 was similar to the procedure shown above, except for the absence of CuTCPP. For TCPP ⊂ UiO-66 (TU), the synthetic process was analogous to the preparation of CTU, except for the substitution of TCPP for CuTCPP.

2.4. Preparation of CuTCPP ⊂ UiO-66/TiO_2 (CTU/TiO_2)

A list of CTU/TiO_2 composites were prepared by in-situ solvothermal process that is similar to the synthesis of CTU (Fig. S3 online) [23]. Typically, TiO_2 particles were dispersed in 2 mL DMF solution and kept stirring. Meanwhile, 30 mg $ZrCl_4$, 30 mg BDC, 10 mg CuTCPP and 0.5 g benzoic acid were successively added to the solution and stirred for 30 min at room temperature. The obtained solution was loaded into 50 mL teflon–lined steel autoclave and heated at 130 °C for 12 h. The final product was collected by centrifugation, washing and ensuing drying in an oven at 80 °C for 12 h. The obtained CTU/TiO_2 samples combined with 0.2, 0.4, 0.6 and 0.8 g TiO_2 were respectively labelled as CTU/0.2TiO_2, CTU/0.4TiO_2, CTU/0.6TiO_2 and CTU/0.8TiO_2.

2.5. Characterizations

The morphology and structure of all composites were observed by JSM-6701E scanning electron microscope (SEM) and JEM2010 EX microscope transmission electron microscopy (TEM). X-ray diffraction (XRD) data were recorded on a Rigaku D/Max–2400/PC with scattering angle ranging from 2° to 60°. Fourier transform infrared (FT-IR) spectroscopy was conducted on a Nicolet NEXUS 670 spectrometer. Diffuse reflectance spectra (DRS) were measured by PuXin TU-1901 UV–vis spectrophotometer equipped with an integrating sphere attachment. The photoluminescence (PL) spectrum detection of samples were conducted on Fluoro Sens 9003 Fluorescence Spectrophotometer. XPS analysis was recorded on PHI5702 photoelectron spectrometer. BET isotherms were obtained with Autosorb-iQ2-MP Sorptometer, the samples were degassed at 120 °C. Measurements of photoelectrochemical (PEC) performance were evaluated on CHI 660D electrochemical workstation. The samples were dissolved in ethanol and adhered to conductive FTO glasses with film solution.

2.6. Photocatalytic reaction procedures

Photocatalytic CO_2 reduction was conducted in 50 mL closed gas stainless–steel reactor settling in a circulation cold water bath system equipped with 300 W Xe lamp ($\lambda > 300$ nm, Beijing Au light Co., Ltd. CEL–HXF300/CEL–HXUV300). During each run, 2 mL distilled H_2O was first filled into a stainless-steel reactor. A quartz glass bottle (40 mm × 25 mm) loaded with 0.1 g catalyst was afterwards encased in the reactor. The reaction setup was purged by pure CO_2 gas (0.1 MPa) and then vacuum-treated more than twice to ensure all the impurities and trapped air were completely removed. During the photocatalytic reduction proceeding, circulating water cooling was used to maintain the reactor at room temperature. The final product was extracted by syringes for further analysis through GC–2080 gas chromatography of flame ionization detector (FID).

2.7. Photoelectrochemical performance

Photoelectrochemical performance measurements were carried out on CHI 660D electrochemical workstation (CHI Shanghai) with typical three electrodes cell under the 300 W Xenon lamp as light source illumination. 0.5 mol L^{-1} Na_2SO_4 was employed as electrolyte. The samples TiO_2 and CTU/0.6TiO_2 were adhered to conductive glasses in a film solution and then dried under infrared light. Three electrodes were working electrode of photoanodes, Ag/AgCl as reference electrode and Pt slice as assistance electrode. All of the measurements were irradiated from the back side of working electrode with about 1 cm^2 areas [24].

3. Results and discussion

The morphologies and microstructures of TiO_2, CTU and CTU/0.6TiO_2 were characterized by SEM and TEM. Pristine TiO_2 nanoparticles exhibit uniform particle morphology but with serious aggregation (Figs. 1a and S7a online). The lattice fringes with spacing of 0.35 nm can be indexed to anatase (1 0 1) crystal plane (Figs. 1f and S8 online). Pure CTU displays sharp edges and smooth surfaces in consistence with octahedral microcrystal morphology (Figs. 1b, S4a–b and S7b online). The SEM and TEM observations of CTU/0.6TiO_2 indicate that the MOF is of great importance in uniformly formatting TiO_2 particles on its external octahedral crystal surface (Fig. 1c–e). Although a slight portion of TiO_2 nanoparticles is observed self-agglomerating, major part of them are evenly scattered on the CTU, suggesting agglomeration of TiO_2 nanoparticles can be effectively prevented. Elemental mappings of CTU/0.6TiO_2 (Fig. S8 online) strongly confirm that the nanocomposite is composed of Zr, Cu, Ti, O, N and C elements. According to the diffraction patterns shown in Fig. S9 (online), it can be found that pristine UiO-66 matches well with previous reports, demonstrating the crystalline structure of UiO-66 is perfectly preserved after the introduction of CuTCPP into the MOF [12]. The XRD of TiO_2 fairly conforms to the HR-TEM for plane of anatase (Fig. S10 online). Also, a low-intensity diffraction peak at angle value 7.17 and 8.35 corresponding to CTU can be seen in the spectra of CTU/TiO_2 (Fig. S11 online). When the mass ratio of CTU in the composites diminishes, this peak intensity weakens accordingly, further justifying a successful combination of CTU and TiO_2.

Due to the comparison between Fourier transform infrared (FT-IR) spectra of UiO-66, TCPP ⊂ UiO-66 (TU) and CuTCPP ⊂ UiO-66 (Figs. 2a and S12 online), the stretching vibrations of Cu-N and OCO of the carboxylic acid that belong to either BDC or porphyrin suggest the presence of CuTCPP compound in the prepared structure [25]. The broad peak located at 3,430 cm^{-1} can be assigned to O-H vibration, which typifies the existence of bound and free water in all samples. As compared to bare UiO-66, the spectra of CTU composites are quite similar, revealing that the backbone of UiO-66 is not affected by the incorporation of either TCPP or CuTCPP. Signals at 1,660 and 1,596 cm^{-1} can be attributed to asymmetric vibrations of carboxyl groups; the peaks at 1,506 and 1,410 cm^{-1} can be identified as symmetric ones [26]. The value of Δv ($\Delta v = v_{as}(COO) - v_s(COO)$) are 154 and 186 cm^{-1}, which are characteristics of the bridge coordination mode of CTU [27]. When the metal Cu^{2+} ions are beset in the ring of TCPP molecules, the newly formed nitrogen ring displays a deformation of the vibration, thus generating Cu-N stretching vibration characteristic at the peak of near 1,000 cm^{-1}. A weak band is detected at 1,660 and 1,596 cm^{-1} in both CTU and CTU/0.6TiO_2 (Fig. 2b and S13 online). It can be assigned to the stretching vibrations of OCO in the carboxylic acid of either BDC or porphyrin.

Analysis of the XPS data can provide information about the composition and chemical state (Fig. S14 online). The CTU/0.6TiO_2 atom percent of C, Cu, N, O, Ti and Zr on the surface of CTU/0.6TiO_2 are 48.47%, 0.47%, 1.51%, 34.87%, 11.11% and 3.58%, respectively. The C 1s spectrum shown in Fig. 3a can be obviously observed by location of two peaks at 284.7 and 288.5 eV, which are attributed to the carboxylate carbon, carbonyl carbon and C=C bond, respectively. As indicated in Fig. 3b, the curves of Zr 3d region can be detected as two peaks for Zr $3d_{5/2}$ and Zr $3d_{3/2}$ at around 182.7 and 185.2 eV, respectively, certifying the existence of Zr^{4+}. As shown in Fig. S15a and b (online), two peaks that appeared at 458.8 and 464.5 eV corresponding to the Ti $2p_{3/2}$ and Ti $2p_{1/2}$ region are in good agreement with the published data. As compared with featured signal Ti $2p_{3/2}$ and Ti $2p_{1/2}$ in TiO_2, the banding energy is reduced by 0.1 eV after incorporation (CTU/0.6TiO_2), sug-

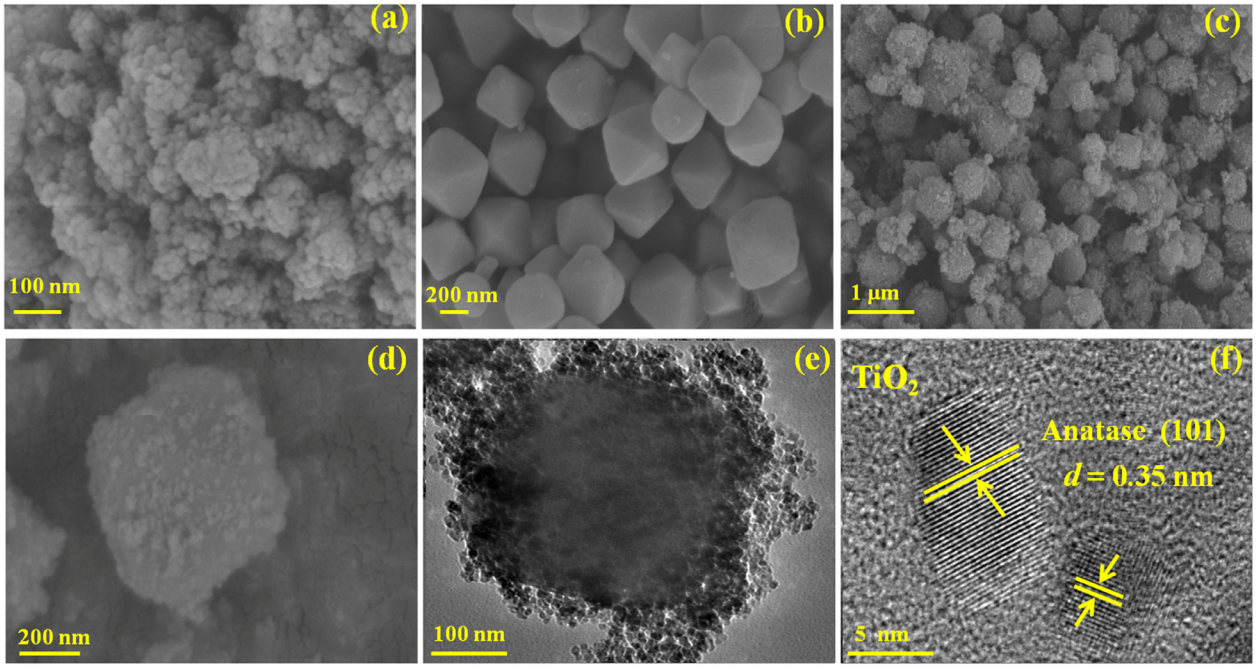

Fig. 1. (Color online) SEM images of (a) TiO_2, (b) CTU, and (c)–(d) CTU/0.6TiO_2. (e) TEM images of CTU/0.6TiO_2. (f) HR–TEM images of TiO_2.

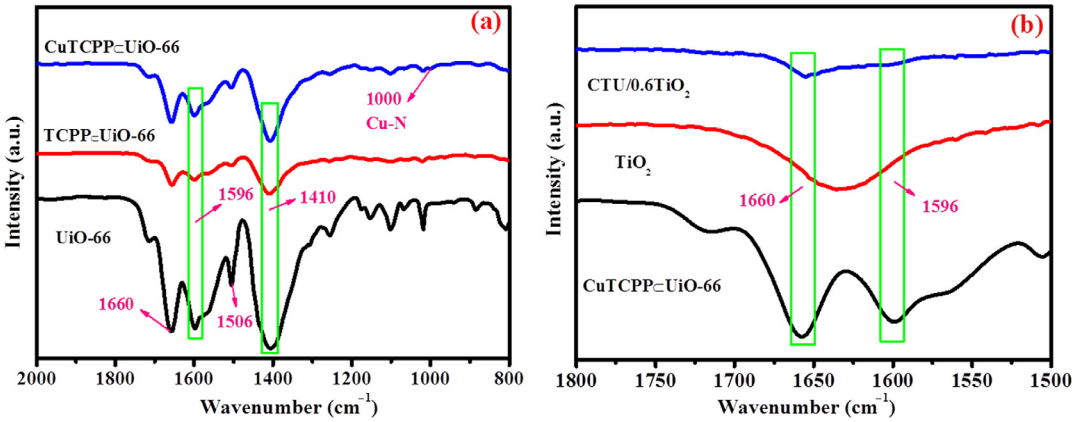

Fig. 2. (Color online) FT–IR spectra of the (a) UiO–66, TCPP ⊂ UiO–66 and CuTCPP ⊂ UiO–66; and (b) CTU/0.6TiO_2, TiO_2 and CuTCPP ⊂ UiO–66.

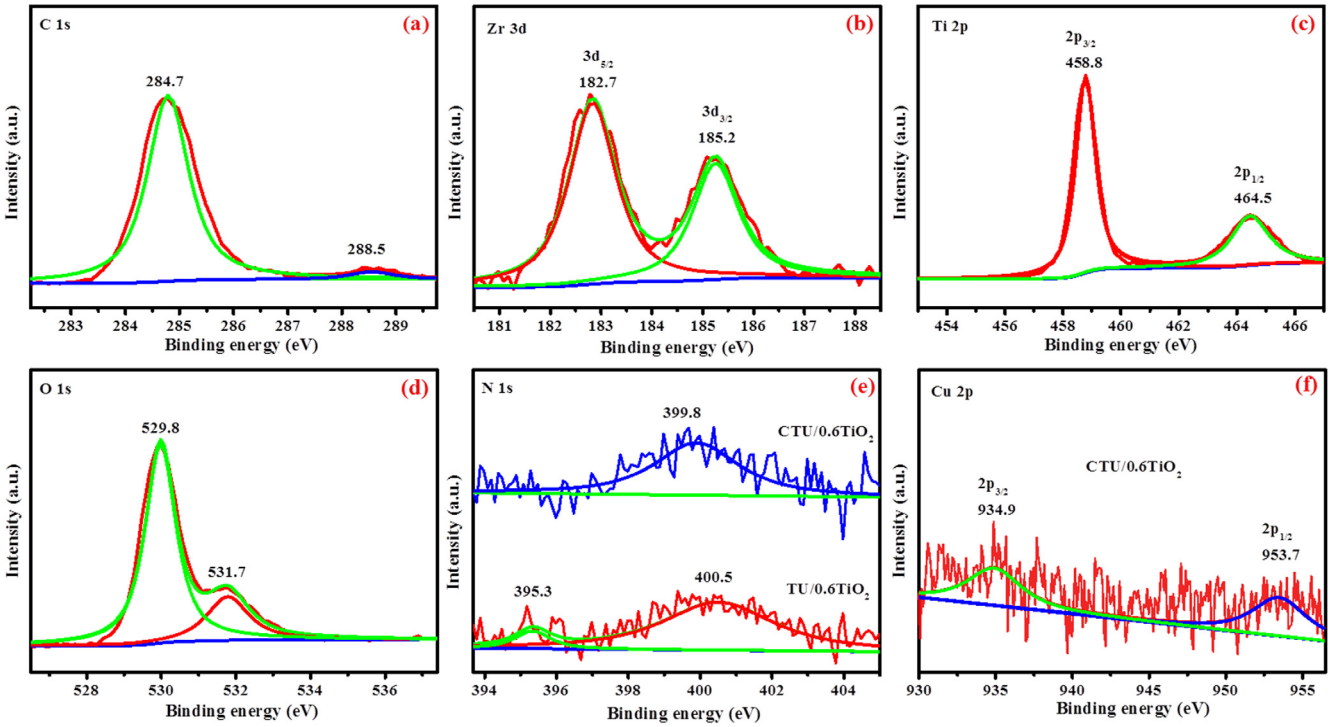

Fig. 3. (Color online) XPS survey spectra of the corresponding samples in high resolution: (a) C 1s (CTU/0.6TiO_2); (b) Zr 3d (CTU/0.6TiO_2); (c) Ti 2p (CTU/0.6TiO_2); (d) O 1s (CTU/0.6TiO_2); (e) N 1s (CTU/0.6TiO_2 and TU/0.6TiO_2); (f) Cu 2p (CTU/0.6TiO_2).

gesting a strong interaction between TiO_2 and the CTU/0.6TiO_2, which might facilitate charge transfer between the two components [28]. The O 1s spectrum (Fig. 3d) gives two peaks at 529.8 and 531.7 eV, implying the existence of O atom in all the composites. Furthermore, the main peak of O 1s XPS for CTU shifts to a 0.3 eV lower position in comparison to that of pure TiO_2 (Fig. S15c online) owning to the existence of oxygen vacancies [29], which would proffer active sites for the CO_2 reduction and suppress the photo-carriers' recombination [17]. Fig. 3e shows the binding energies given by N 1s peaks of CTU/0.6TiO_2 and TU/0.6TiO_2. However, the featured signals of both N and Cu are weak due to their minor content in the composite. The peak at about 395.3 eV of nitrogen disappears after the coordination of Cu ion with the four N atoms. It can be ascribed to the changes in symmetry of chemical environments [30,31]. Fig. 3f indicates that Cu $2p_{3/2}$ and Cu $2p_{1/2}$ are located at 934.9 and 953.7 eV, respectively, further testifying to the successful preparation of CTU [32,33].

The N_2 adsorption-desorption trials were exerted to analyze samples' surface and pore distribution (Figs. 4a, S16 and Table S1 online). The isotherms of the CTU sample exhibit a type I isotherm at 77 K with no hysteresis, illustrating a typical microporous structure. The Horvath-Kawazoe (HK) microspore size distribution of CTU (Fig. 4b) gives three major pores at 1.48, 1.99 and 3.53 nm, respectively. The surface area and pore volume of CTU are 1,023.1 $m^2\ g^{-1}$ and 0.573 $cm^3\ g^{-1}$, respectively. The pure TiO_2 displays type IV isotherm with a discrete hysteresis loop (H3 type) in the high relative pressure range, demonstrating the presence of a mesoporous structure, which may be derived from the egregious agglomeration of TiO_2 nanoparticles. The integration of CTU and TiO_2 provides a higher specific surface area than that of only TiO_2 (Table S1 online). With gradual decrement in the relative content

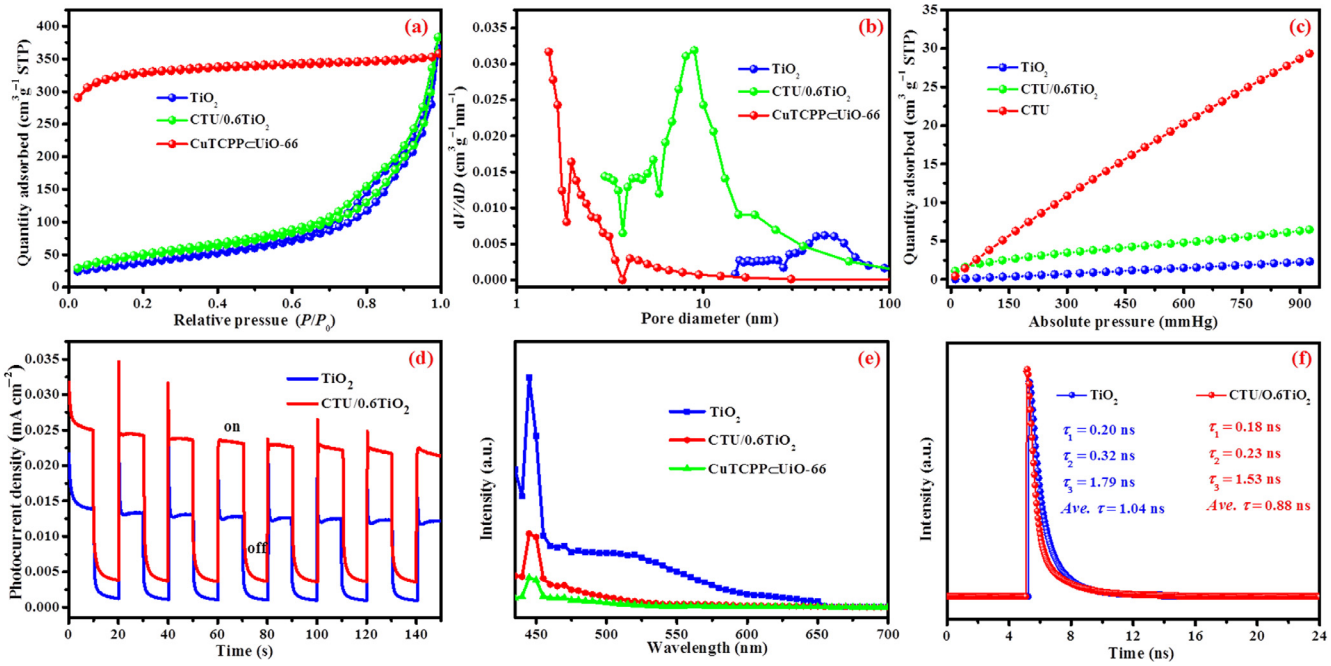

Fig. 4. (Color online) BET adsorption–desorption isotherms (a) and the corresponding pore size distribution (b) of TiO_2, CTU/0.6TiO_2 and CTU. CO_2 sorption isotherms measured at 25 °C (c) for TiO_2, CTU/0.6TiO_2 and CTU. Photocurrent–time (*I*-*t*) curves (d) of TiO_2 and CTU/0.6TiO_2. PL spectra (e) of the various components at 415 nm excitation. Time-resolved PL spectra (f) of TiO_2 and CTU/0.6TiO_2.

of CTU, the surface area (S_{BET}) of the composite accordingly diminishes. Generally, surface area based on the total weight of the nanocomposite is significantly lower than that of the pure CTU [34].

To investigate the incorporation mode of CuTCPP in CTU, N_2 adsorption-desorption detections for UiO-66 and CTU were operated in prior. Associating with the significant decrement in adsorption capacity and pore size distribution of CTU in comparison to that of UiO-66 (Fig. S17 online), it is considered that CuTCPP occupies the pores of the structure, and might bond through the coordination between the carboxyl (—COOH) in CuTCPP and the Zr_6 in UiO-66. This integral structure is similar to the reported MOF, in which CuTCPP is substituted by Ni porphyrin. Moreover, an operation was carried out by directly mixing UiO-66 and copper porphyrin to engender post–modified UiO-66 (PMU, the detailed procedure can be seen in Fig. S18 online). Consequently, both the obtained PMU and CTU were further digested by 16% HF solution to conduct ^{1}H NMR comparison between the resulted compounds, and give a precise investigation on the integrating modality. ^{1}H NMR analysis of the products resulted from CTU digestion shows a strong characteristic signal of BDC (δ 8.00 ppm) as well as that of CuTCPP (δ 8.25, 8.75 ppm, Figs. S18 and S19 online). By contrast, the compounds generated by digesting PMU only presents the featured signal of BDC, suggesting that the simply adsorbed or encapsulated CuTCPP in/on UiO-66 is washed away during the preparation process due to its weak bonding. To further confirm the consideration, CuTCPP was substituted by Cu(II) tetrakis(4-phenyl)porphyrin (Cu-TPP) in analogous size to oprerate the same preparation procedure. In the absence of coordinative substituent —COOH, the achieved structure is easily washed from red into white color (Fig. S20 online). In contrast, the color of CuTCPP ⊂ UiO-66 can be hardly washed away. Associating with previous study [12], it is thereby ascertained that the primary portion of CuTCPP displays steady coordination mofde in the CTU structure.

In comparison to pure TiO_2, the CO_2 adsorption curves in Fig. 4c presents an enhanced adsorption capacity, which might be led by the existence of the micropores in CTU. It is considered that MOF can provide enlarged surface area and consequently present increased capability to adsorb the substrate CO_2 in comparison to pure TiO_2 [35]. The photocurrent-time (*I*-*t*) curves (Fig. 4d) reveal that the photocurrent intensity is significantly enhanced by the in-situ growth of of TiO_2 onto CTU in comparison to either component alone. The recombination of light-triggered carriers is also greatly abated. To concretely verify the integral effect of the composite on the separation of carriers, photoluminescence (PL) measurements were carried out. Fluorescence quenching discerned in Fig. 4e clearly unveils that CTU is able to effectively suppress the recombination of photo-generated electrons and holes [36,37]. Compared to TiO_2, the fluorescence intensity of CTU/0.6TiO_2 is dramatically reduced, resultantly highly raising the efficiency of carrier transfer. The average PL lifetime has been commonly regarded as a crude indicator to estimate the separation efficiency of photo-excited carriers [38]. In this regard, time-resolved PL detection was exerted (Fig. 4f). A shortened lifetime of 0.16 ns from TiO_2 to CTU/0.6TiO_2 further confirms the promotive effect of CTU on separation of the photo-induced carriers.

The photocatalysis conducted by as-prepared multiple functionalities CTU/TiO_2 composites were evaluated under 300 W Xe lamp irradiation ($\lambda > 300$ nm). As shown in Fig. 5a, the composites with different amounts of grown TiO_2 nanoparticles generate various CO_2 conversions. Among the as-prepared composites, CTU/0.6TiO_2 presents the optimal value of 31.32 μmol g^{-1}h^{-1} CO and 0.148 μmol g^{-1}h^{-1} CH_4 evolution amount. The yield of CO product is about 7 times higher than that produced by pure TiO_2. With respect to the performance of the TiO_2-based materials (Fig. 5), all nanocomposites show superior photoactivity rather than the pure TiO_2 mainly due to a synergistic effect between TiO_2 and CTU, i.e., consistent augment of light absorption as well as combination between MOF and TiO_2, both of which will be elaborately demonstrated in mechanism as given below. In addition, the enhanced dispersion of TiO_2 NPs by MOF is also able to prevent TiO_2 particle from aggregation and consequently provide additional exposed surface reaction sites [6,34]. Hence, when the amount of CTU in the composite is fixated, the catalytic activity can be continuously improved along with increasing the amount of the loaded primary

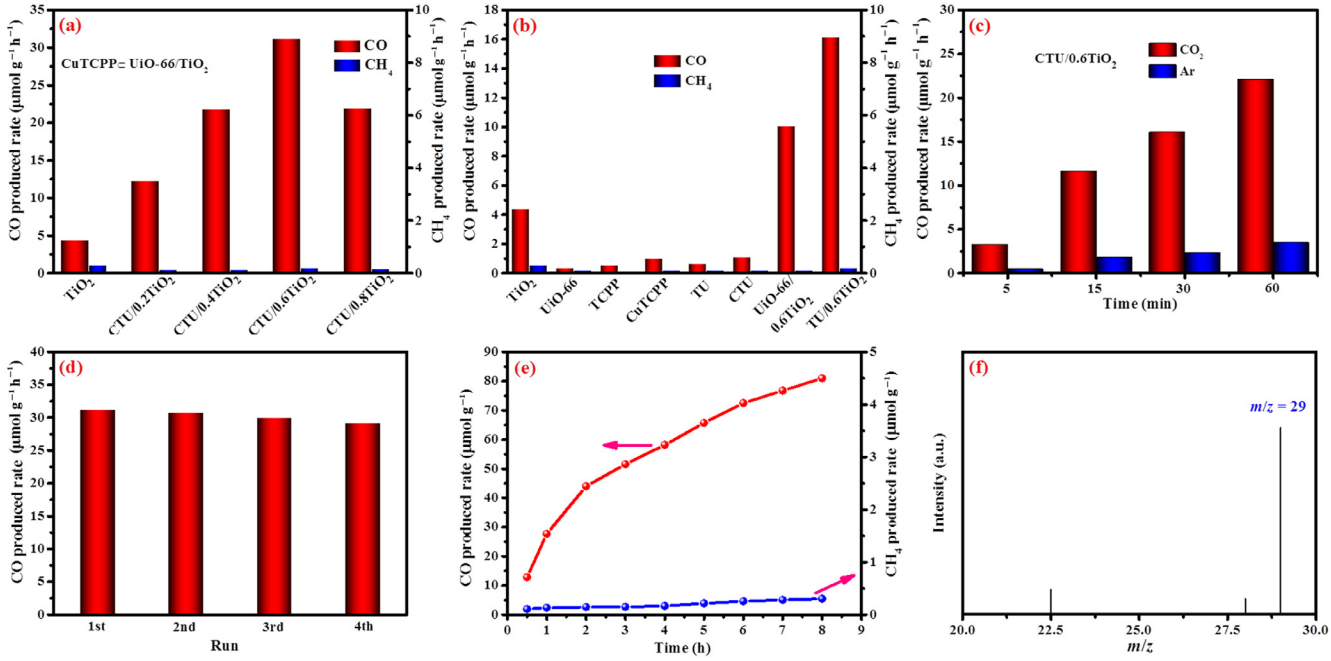

Fig. 5. (Color online) Dependence of total CO/CH_4 evolution on the amount (a) of TiO_2 and different ratio CTU/TiO_2 with Xe lamp irradiation ($\lambda > 300$ nm) within 1 h. Controlled experiments (b) employing all the as-prepared photocatalysts with Xe lamp irradiation within 1 h. Total CO evolution amount (c) over CTU/0.6TiO_2 (Xe lamp) within 1 h in the atmosphere of CO_2 and Ar. Four cycles (d) of CO_2 reduction over the CTU/0.6TiO_2. Total CO/CH_4 evolution amount (e) given by CTU/0.6TiO_2 with Xe lamp within 8 h. GC–MS spectra ($m/z = 29$) analyses (f) of generated CO by CTU/0.6TiO_2 with $^{13}CO_2$ as carbon source.

catalyst, TiO_2 (Fig. 5a). Nonetheless, when the proportion of TiO_2 in the composite is over 0.6, the surplus TiO_2 NPs would aggregate on the surface of CTU and generate disfavored effect on the photocatalytic performance. The evolution ratio of CO to CH_4 conducted by TiO_2 was 14.67, whereas the ratio generated from CTU/0.6TiO_2 was 173.39, unveiling an extraordinarily improved selectivity for yielding CO after combination. It is considered that both the enhanced photon efficiency and strengthened binding affinity of active sites toward CO_2 molecules result in this great improvement as compared to pure TiO_2 [39,40].

In order to compare catalytic abilities of the composite and the corresponding components, a series of controlled experiments were carried out (Fig. 5b). After 1 h reaction under identical conditions, the composites CTU/TiO_2 perform better catalytic activity than either using CTU or TiO_2 alone. After four cycles of photocatalysis, negligible decrement in CO evolution can be observed, indicating an approving recyclability of CTU/TiO_2 (Fig. 5d). When the light irradiation lasted for 8 h, the photocatalysis conducted by CTU/0.6TiO_2 presents continuously increasing yields of both CO and CH_4, suggesting that the photocatalyst of CTU/0.6TiO_2 keeps active during the entire test (Fig. 5e). To identify the origin carbon source of the generated CO, the produced CO from the isotopic experiment ($^{13}CO_2$) was analyzed by GC–MS. As shown in Fig. 5f, the $m/z = 29$ resulted from GC–MS analysis can be assigned to ^{13}CO. This study provides a concrete proof that the generated CO is mainly derived from extraneously introduced carbon dioxide. In addition, with respect to the spectra of *I-t*, FT-IR and XRD, the quite similarity between pristine CTU/0.6TiO_2 and used one illustrates that CuTCPP's structure composition still sustains well after long-time or recycling photocatalytic process (Figs. S23–S25 online).

For the purpose of deeply demonstrating the combination effects on the ameliorated photocatalytic performance, UV–vis diffuse reflectance spectra were implemented. As shown in Fig. 6a, a significant red shift of absorption edge can be observed after the introduction of CuTCPP into UiO-66, suggesting light-harvesting CuTCPP is capable of raising the light absorption of UiO-66. Compared with TiO_2, the absorption edge of CTU/TiO_2 rarely moves. By contrast, the absorption intensities of the samples after combination dramatically increase in visible light region. It might

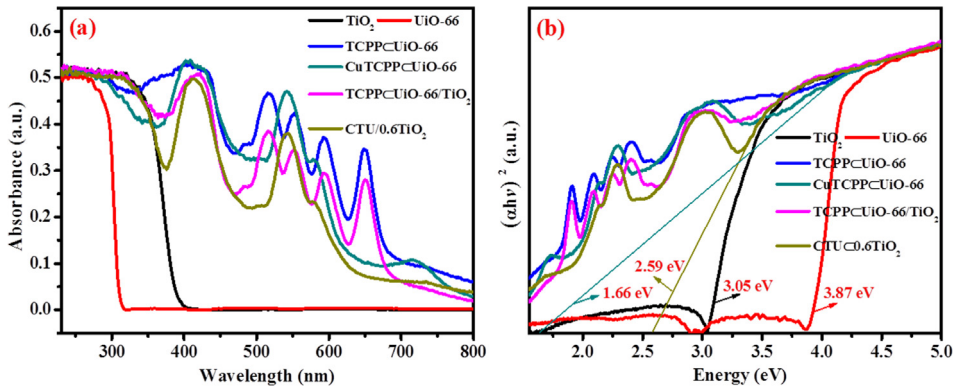

Fig. 6. (Color online) UV–vis diffuse reflectance spectra (a) and estimation of band gap energies (b) of the as-synthesized samples.

be ascribable to the integration of either TCPP or CuTCPP into UiO-66, which maintains great capability of absorbing solar light. On the part of TU/TiO_2, there are five absorption peaks in visible region. Whereas, the coordination of Cu^{2+} ions with the nitrogen atoms in TCPP can result in an enhanced spatial symmetry for CTU/TiO_2, manifesting as only one absorption peak in visible region. According to previous study [41], CuTCPP can form the ligand-to-metal charge transfer (LMCT) in comparison to mere TCPP. The energy transfer between the ligands and metal center can take advantageous effect on the photocatalytic reactions [42]. Moreover, the tangents of $(\alpha hv)^2$ vs. photon energy were employed to estimate band-gap energy (Fig. 6b). CuTCPP plays a significant role in the light-absorption properties of nanocomposites, leading to an obvious reduction of band gap from 1.66 eV for CTU and 3.05 eV for TiO_2 to 2.59 eV of CTU/TiO_2 after growing TiO_2 on the MOF. Undetectable adsorption of either neat UiO-66 or TiO_2 in the visible region can be attributed to their large band gap of 3.87 and 3.05 eV, respectively. Hence, integration of CuTCPP with UiO-66 via introducing mixed-linker approach can bring up a new energy level that narrows the original band-gap energy of UiO-66 [43–46].

In addition, the potential position of CTU was measured by Motty-Schottky (M-S) curves (Figs. S26 and S27 online). The positive slope indicates that both functionalized MOF and TiO_2 are n-type semiconductors. According to the curve (M-S), the flat band potential of CTU is approximately −0.6 eV vs. Ag/AgCl. The DRS exhibits that the band gap value is 1.66 eV, giving the LUMO and HOMO positions of CTU at −0.6 and 1.06 eV, respectively. The conduction band (CB) level of TiO_2 is −0.3 eV while its band gap value is 3.05 eV. Therefore, the valence band (VB) potential of TiO_2 was calculated as 2.75 eV. Compared with the LUMO of CTU, the CB of TiO_2 is much more positive, resultantly confirming the facilitation to the separation of electron-hole pairs by the formation of composites [47].

Based on the characterization and photocatalytic performance mentioned above, a possible light absorption mechanism and efficient electron-hole separation of CTU/TiO_2 was proposed in Fig. 7 [11]. When irradiated by Xe lamp light, both the composed part, CTU and TiO_2 were excited to generate electron-hole pairs. Since the LUMO potential of CTU is more negative than the CB potential of TiO_2, the photo-induced electrons on the LUMO of CTU are able to directly transfer to the CB of TiO_2 [48]. In the photocatalytic CO_2 reduction, in addition to transferring to the HOMO energy level of CTU so as to reduce the charge recombination, the photo-induced holes generated in VB of TiO_2 can also oxidize H_2O to produce ·OH radicals, which would further release O_2 and H^+ [34,49]. As indicated by the slight generation of carbon-based derivatives during the 1 h irradiation without introducing exotic carbon dioxide in the reactor, the hydroxyl radical might also oxidize the organic component in the composite (Figs. 5c and S28 online). According to the carbon isotopic trace of CO_2 and enduring recycling test of CTU/TiO_2, the carbon source primarily is derived from extraneous CO_2 during the photocatalytic reduction, and the decomposition of photocatalyst is relatively negligible.

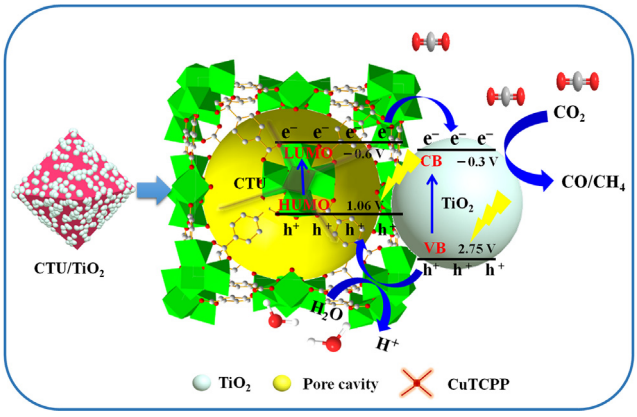

Fig. 7. (Color online) Proposed photocatalytic CO_2 reduction pathway over CTU/TiO_2.

4. Conclusions

In summary, CTU/TiO_2 composite photocatalysts have been successfully prepared by the hydrothermal in-situ growth method. The resultant hybrids exhibit significantly ameliorated photocatalytic activity for CO_2 reduction compared with either pristine TiO_2 or CTU. The optimum loading content of CTU is determined as CTU/0.6TiO_2, the employment of which can give CO production rate as 31.32 μmol $g^{-1}h^{-1}$ and CH_4 genration as 0.148 μmol $g^{-1}h^{-1}$. The composite photocatalyst CTU/0.6TiO_2 presents 7-fold-enhanced CO_2-to-CO conversion activity in comparison to the pristine TiO_2. The improved photocatalytic ability after combination could be primarily ascribable to the enhanced separation of the photogenerated charges. Besides, the CTU MOF is able to greatly meliorate the dispersion of TiO_2 particles, resultantly providing sufficient exposure of reactive sites with ameliorated ability of capturing CO_2 as compared with pristine TiO_2. Additionally, the as-prepared CTU/TiO_2 composites display highly stable recyclability during photocatalytic reduction of CO_2. The outcome of this work provides new insights into rational design of MOF-based hybrid nanomaterials for efficient photo-reduction of CO_2.

Conflict of interest

The authors declare that they have no conflict of interest.

Acknowledgments

This work was financially supported by the National Natural Science Foundation of China (21663027, 21808189) and the Science and Technology Support Project of Gansu Province (1504GKCA027).

Author contributions

L.W. designed the hybrid structure. L.W. and P.X.J. prepared the catalysts and conducted the sample characterization. L.W., P.X.J. and S.H.D. performed photocatalytic performance and data analysis. L.W., H.D.S. and J.W.H. discussed the corresponding mechanism. H.D.S. and Q.Z.W. conceived and led the project. Q.Z.W. supported and supervised the research. All authors made contribution to technical discussions and paper writing.

Appendix A. Supplementary data

Supplementary data to this article can be found online at https://doi.org/10.1016/j.scib.2019.05.012.

References

[1] Marszewski M, Cao S, Yu J, et al. Semiconductor-based photocatalytic CO_2 conversion. Mater Horiz 2015;2:261–78.
[2] Son HJ, Jin S, Patwardhan S, et al. Light-harvesting and ultrafast energy migration in porphyrin-based metal-organic frameworks. J Am Chem Soc 2013;135:862–9.
[3] Liu X, Inagaki S, Gong J. Heterogeneous molecular systems for photocatalytic CO_2 reduction with water oxidation. Angew Chem Int Ed Engl 2016;55:14924–50.
[4] Lee CY, Farha OK, Hong BJ, et al. Light-harvesting metal-organic frameworks (MOFs): efficient strut-to-strut energy transfer in bodipy and porphyrin-based MOFs. J Am Chem Soc 2011;133:15858–61.

[5] Wang S, Wang X. Imidazolium ionic liquids, imidazolylidene heterocyclic carbenes, and zeolitic imidazolate frameworks for CO_2 capture and photochemical reduction. Angew Chem Int Ed Engl 2016;55:2308–20.
[6] Xu HQ, Yang S, Ma X, et al. Unveiling charge-separation dynamics in CdS/metal-organic framework composites for enhanced photocatalysis. ACS Catal 2018;8:11615–21.
[7] Lee Y, Kim S, Kang JK, et al. Photocatalytic CO_2 reduction by a mixed metal (Zr/Ti), mixed ligand metal-organic framework under visible light irradiation. Chem Commun 2015;51:5735–8.
[8] Jiao L, Wan G, Zhang R, et al. From Metal-organic frameworks to single-atom Fe implanted N-doped porous carbons: efficient oxygen reduction in both alkaline and acidic media. Angew Chem Int Ed Engl 2018;57:8525–9.
[9] Sun D, Gao Y, Fu J, et al. Construction of a supported Ru complex on bifunctional MOF-253 for photocatalytic CO_2 reduction under visible light. Chem Commun 2015;51:2645–8.
[10] Xu HQ, Hu J, Wang D, et al. Visible-light photoreduction of CO_2 in a metal-organic framework: boosting electron-hole separation via electron trap states. J Am Chem Soc 2015;137:13440–3.
[11] Dhakshinamoorthy A, Asiri AM, Garcia H. Metal-organic framework (MOF) compounds: photocatalysts for redox reactions and solar fuel production. Angew Chem Int Ed Engl 2016;55:5414–45.
[12] Sun Y, Sun L, Feng D, et al. An in situ one-pot synthetic approach towards multivariate zirconium MOFs. Angew Chem Int Ed Engl 2016;55:6471–5.
[13] Wang B, Lv XL, Feng D, et al. Highly stable Zr(IV)-based metal-organic frameworks for the detection and removal of antibiotics and organic explosives in water. J Am Chem Soc 2016;138:6204–16.
[14] Rosser TE, Windle CD, Reisner E. Electrocatalytic and solar-driven CO_2 reduction to CO with a molecular manganese catalyst immobilized on mesoporous TiO_2. Angew Chem Int Ed Engl 2016;55:7388–92.
[15] Wang C, Xie Z, deKrafft KE, et al. Doping metal-organic frameworks for water oxidation, carbon dioxide reduction, and organic photocatalysis. J Am Chem Soc 2011;133:13445–54.
[16] Kong ZC, Liao JF, Dong YJ, et al. Core@Shell $CsPbBr_3$@Zeolitic imidazolate framework nanocomposite for efficient photocatalytic CO_2 reduction. ACS Energy Lett 2018;3:2656–62.
[17] She HD, Zhou H, Li LS, et al. Nickel-doped excess oxygen defect titanium dioxide for efficient selective photocatalytic oxidation of benzyl alcohol. ACS Sustain Chem Eng 2018;6:11939–48.
[18] Kim C, Cho KM, Al-Saggaf A, et al. Z-scheme photocatalytic CO_2 conversion on three-dimensional $BiVO_4$/carbon-coated Cu_2O nanowire arrays under visible light. ACS Catal 2018;8:4170–7.
[19] Ma K, Yehezkeli O, Domaille DW, et al. Enhanced hydrogen production from DNA-assembled Z-Scheme TiO_2-CdS photocatalyst systems. Angew Chem Int Ed Engl 2015;54:11490–4.
[20] Maina JW, Pozo-Gonzalo C, Kong L, et al. Metal organic framework based catalysts for CO_2 conversion. Mater Horiz 2017;4:345–61.
[21] Aguirre ME, Zhou R, Eugene AJ, et al. Cu_2O/TiO_2 heterostructures for CO_2 reduction through a direct Z-scheme: protecting Cu_2O from photocorrosion. Appl Catal B Environ 2017;217:485–93.
[22] Wang L, Duan SH, Jin PX, et al. Anchored Cu(II) tetra(4-carboxylphenyl)porphyrin to P25 (TiO_2) for efficient photocatalytic ability in CO_2 reduction. Appl Catal B Environ 2018;239:599–608.
[23] Xu J, Gao J, Wang C, et al. NH_2-MIL-125(Ti)/graphitic carbon nitride heterostructure decorated with NiPd co-catalysts for efficient photocatalytic hydrogen production. Appl Catal B Environ 2017;219:101–8.
[24] Wang Q, He J, Shi Y, et al. Designing non-noble/semiconductor Bi/$BiVO_4$ photoelectrode for the enhanced photoelectrochemical performance. Chem Eng J 2017;326:411–8.
[25] Zhang TZ, Lu Y, Li YG, et al. Metal-organic frameworks constructed from three kinds of new Fe-containing secondary building units. Inorg Chim Acta 2012;384:219–24.
[26] Wang H, Yin F, Li G, et al. Preparation, characterization and bifunctional catalytic properties of MOF(Fe/Co) catalyst for oxygen reduction/evolution reactions in alkaline electrolyte. Int J Hydrogen Energy 2014;39:16179–86.
[27] Chen C, Chen D, Xie S, et al. Adsorption behaviors of organic micropollutants on zirconium metal-organic framework UiO-66: analysis of surface interactions. ACS Appl Mater Interfaces 2017;9:41043–54.
[28] Yan S, Ouyang S, Xu H, et al. Co-ZIF-9/TiO_2 nanostructure for superior CO_2 photoreduction activity. J Mater Chem A 2016;4:15126–33.
[29] Zhang D, Ma X, Zhang H, et al. Enhanced photocatalytic hydrogen evolution activity of carbon and nitrogen self-doped TiO_2 hollow sphere with the creation of oxygen vacancy and Ti^{3+}. Mater Today Energy 2018;10:132–40.
[30] Usov PM, Huffman B, Epley CC, et al. Study of electrocatalytic properties of metal-organic framework PCN-223 for the oxygen reduction reaction. ACS Appl Mater Interfaces 2017;9:33539–43.
[31] Liu Y, Yang Y, Sun Q, et al. Chemical adsorption enhanced CO_2 capture and photoreduction over a copper porphyrin based metal organic framework. ACS Appl Mater Interfaces 2013;5:7654–8.
[32] He X, Wang WN. MOF-based ternary nanocomposites for better CO_2 photoreduction: roles of heterojunctions and coordinatively unsaturated metal sites. J Mater Chem A 2018;6:932–40.
[33] Han X, He X, Sun L, et al. Increasing effectiveness of photogenerated carriers by in situ anchoring of Cu_2O nanoparticles on a nitrogen-doped porous carbon yolk–shell cuboctahedral framework. ACS Catal 2018;8:3348–56.
[34] Crake A, Christoforidis KC, Kafizas A, et al. CO_2 capture and photocatalytic reduction using bifunctional TiO_2/MOF nanocomposites under UV-vis irradiation. Appl Catal B Environ 2017;210:131–40.
[35] Cao S, Shen B, Tong T, et al. 2D/2D heterojunction of ultrathin MXene/Bi_2WO_6 nanosheets for improved photocatalytic CO_2 reduction. Adv Funct Mater 2018;28:1800136.
[36] Wang S, Lin J, Wang X. Semiconductor-redox catalysis promoted by metal-organic frameworks for CO_2 reduction. Phys Chem Chem Phys 2014;16:14656–60.
[37] Li X, Pi Y, Hou Q, et al. Amorphous TiO_2@NH_2-MIL-125(Ti) homologous MOF-encapsulated heterostructures with enhanced photocatalytic activity. Chem Commun 2018;54:1917–20.
[38] Zhou M, Wang S, Yang P, et al. Boron carbon nitride semiconductors decorated with CdS nanoparticles for photocatalytic reduction of CO_2. ACS Catal 2018;8:4928–36.
[39] Liu B, Ye L, Wang R, et al. Phosphorus-doped graphitic carbon nitride nanotubes with amino-rich surface for efficient CO_2 capture, enhanced photocatalytic activity, and product selectivity. ACS Appl Mater Interfaces 2018;10:4001–9.
[40] Diercks CS, Liu Y, Cordova KE, et al. The role of reticular chemistry in the design of CO_2 reduction catalysts. Nat Mater 2018;17:301–7.
[41] Ryland ES, Lin MF, Verkamp MA, et al. Tabletop femtosecond M-edge X-ray absorption near-edge structure of FeTPPCl: metalloporphyrin photophysics from the perspective of the metal. J Am Chem Soc 2018;140:4691–6.
[42] Huang YB, Liang J, Wang XS, et al. Multifunctional metal-organic framework catalysts: synergistic catalysis and tandem reactions. Chem Soc Rev 2017;46:126–57.
[43] Ge R, Li X, Zhuang B, et al. Assembly mechanism and photoproduced electron transfer for a novel cubic Cu_2O/tetrakis(4-hydroxyphenyl)porphyrin hybrid with visible photocatalytic activity for hydrogen evolution. Appl Catal B Environ 2017;211:296–304.
[44] Zhang Z, Liu H, Xu J, et al. Enhancing the visible light absorption and charge separation of Bi_2WO_6 by hybridizing a CuTCPP sensitizer. Photochem Photobiol Sci 2017;16:1194–200.
[45] Wang QZ, Niu TJ, Wang L, et al. $FeF_2/BiVO_4$ heterojuction photoelectrodes and evaluation of its photoelectrochemical performance for water splitting. Chem Eng J 2018;337:506–14.
[46] She HD, Li LS, Sun YD, et al. Facile preparation of mixed-phase CdS and its enhanced photocatalytic selective oxidation of benzyl alcohol under visible light irradiation. Appl Surf Sci 2018;457:1167–73.
[47] Wang QZ, He JJ, Shi YB, et al. Synthesis of MFe_2O_4 (M=Ni, Co)/BiV_O4 film for photolectrochemical hydrogen production activity. Appl Catal B Environ 2017;214:158–67.
[48] Li R, Hu J, Deng M, et al. Integration of an inorganic semiconductor with a metal-organic framework: a platform for enhanced gaseous photocatalytic reactions. Adv Mater 2014;26:4783–8.
[49] Shi L, Wang T, Zhang H, et al. Electrostatic self-assembly of nanosized carbon nitride nanosheet onto a zirconium metal-organic framework for enhanced photocatalytic CO_2 reduction. Adv Funct Mater 2015;25:5360–7.

Lei Wang received his B.S. degree in chemistry from Jilin University (2006). Then he obtained his Ph.D. degree in 2012 under the supervision of Prof. Ning Tang in Lanzhou University before working at Northwest Normal University as an Associate Professor. During 2015–2016, he worked as Visiting Scholar in Dr. John Yang's group at Missouri University. His research interests mainly focus on developing inorganic-organic hybrids for photocatalytic CO_2 reduction and contaminant degradation.

Qizhao Wang is a Professor at Northwest Normal University. His current research interests primarily center on exploring novel inorganic semiconductors to execute photo/electro-photo catalysis for water splitting, CO_2 reduction and contaminant degradation.